Inorganic Chemistry
Article
pubs.acs.org/IC

Structural, Electronic, and Ferroelectric Properties of Compressed $CdPbO_3$ Polymorphs

Yuanhui Xu,[†] Xianfeng Hao,[†,‡] Cesare Franchini,[‡] and Faming Gao*,[†]

[†]Key Laboratory of Applied Chemistry, Yanshan University, Qinhuangdao 066004, China
[‡]Faculty of Physics and Center for Computational Materials Science, University of Vienna, A-1090 Vienna, Austria

Supporting Information

ABSTRACT: By means of first-principles calculations based on density functional theory (DFT) and hybrid functional, we studied the structural, electronic, and ferroelectric properties of the two recently synthesized high-pressure perovskite-type (orthorhombic, space group *Pnma*) and $LiNbO_3$-type (rhombohedral, space group *R*3*c*) polymorphs of $CdPbO_3$. Besides providing structural and electronic results in good agreement with available experiments, our results are able to correctly describe the pressure-induced *Pnma* → *R*3*c* structural phase transition and most importantly predict the realization of proper ferroelectric behavior in $LiNbO_3$-type $CdPbO_3$ with an electric polarization of 52.3 $\mu C/cm^2$. The proper covalent interaction mechanism driving the ferroelectric transition is discussed and explained in terms of the analysis of Born effective charges, potential-energy surfaces, charge density isosurfaces, and electric localization function.

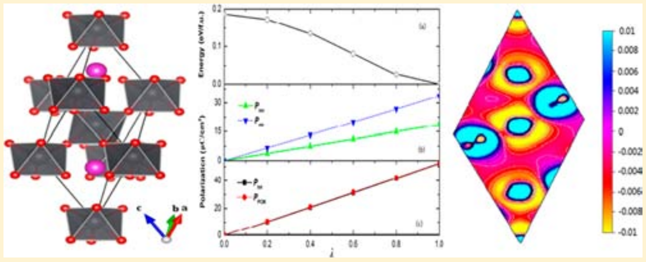

I. INTRODUCTION

Perovskite-structure oxides with general formula ABO_3 are known to exhibit a wide variety of physical properties such as high dielectric constant, ferroelectric polarization, colossal magnetoresistance, and superconductivity. For this reason they form one of the most important classes of materials for technological applications. In particular, perovskite compounds display a large degree of structural freedom depending on the relative size of the A and B ions and on the mismatch between the A−O and the B−O equilibrium bond lengths. As a result of this structural flexibility, a wide variety of distorted variants of the prototypical cubic structure are observed as a function of compositions and, also, external perturbations such as temperature and pressure. The physical behavior of perovskite oxides depends crucially on the details of these distortions, particularly the electronic, magnetic, and dielectric properties.

The prototypical perovskite has cubic structure with $Fm\bar{3}m$ symmetry, and it can be described as a framework of corner-sharing BO_6 octahedra with the A cations located at the 12-fold-coordinated voids within the octahedra. The stability and distortion of perovskite crystal structures are often discussed in terms of the Goldschmidt's tolerance factor *t*, $t = (r_A + r_O)/\sqrt{2}(r_B + r_O)$, where r_A, r_B, and r_O are the ionic radii of A, B, and O ions, respectively.[1,2] $t = 1$ represents the ideal conditions upon which the perovskite structure assumes its ideal cubic symmetry. Depending on whether the tolerance factor *t* is greater or less than 1, different distorted structural variants are formed. However, the tolerance factor of perovskite is not the only predominant factor to determine the stability of a given compound. As a means to alter the electronic bonding state, the lattice, and thus the physical properties of perovskite compounds, high pressure has been widely used in geoscience and related fields to provide access to new phases, unstable or metastable at ambient pressure conditions, which may display novel and fundamentally relevant physical properties.[3]

Recently, Inaguma et al.[4,5] reported two high-pressure polymorphs of the transition metal perovskites $PbNiO_3$ and $CdPbO_3$ characterized by distinct crystal structures: (i) an orthorhombic perovskite type with space group *Pnma* and (ii) a hexagonal lithium niobate ($LiNbO_3$)-type (LNO) structure with space group *R*3*c*. In situ energy-dispersive X-ray diffraction (XRD) experiment revealed that in $PbNiO_3$ the *Pnma* phase is formed at 400 °C under a pressure of 3 GPa and that the perovskite-type phase irreversibly transforms to the LNO-type phase by heat treatment at ambient pressure.[4] At variance with $PbNiO_3$, synthesis of the perovskite-type or LNO-type phases in compressed $CdPbO_3$ strongly depends on heating temperature: XRD patterns showed that the *Pnma* phase is formed under 7 GPa and at a heating temperature of 750 °C and the LNO-type phase at 1200 and 1300 °C. It has been also shown that both phases can coexist in the temperature range 750−1000 °C.[5]

Apart from their relative stability, the *Pnma* (orthorhombic perovskite-type) and *R*3*c* (hexagonal LNO-type) phases exhibit interesting electronic properties. Particularly intriguing is the physical properties of the LNO-type structure. In fact, the *R*3*c* symmetry allows development of spontaneous polarization along the [111] direction and, as such, may give rise to ferroelectricity, piezoelectricity, pyroelectricity, and second-

Received: October 19, 2012
Published: January 9, 2013

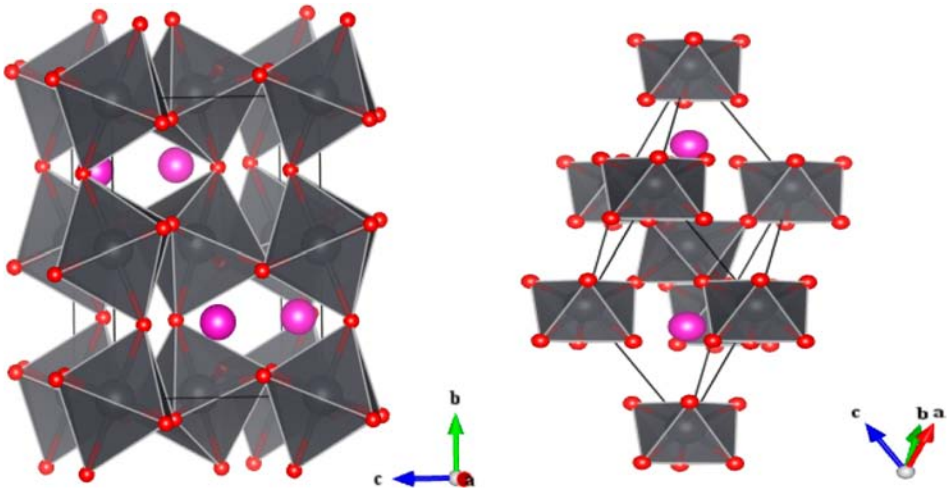

Figure 1. Crystal structures of the perovskite-type (left) and $LiNbO_3$-type (right, shown in the rhombohedral setting) $CdPbO_3$. Magenta (medium), black (large), and red (small) spheres represent Cd, Pb, and O atoms, respectively. Octahedron centered at one Pb atom is shown in both structures.

order nonlinear optical behavior.[6,7] For example, the well-known LNO-type oxides $LiNbO_3$ and $LiTaO_3$ exhibit excellent ferroelectric properties,[8,9] and $BiFeO_3$ is one of the most renowned multiferroic compounds.[10−12] Indeed, on the basis of beyond density functional theory (DFT) calculations, some of us recently predicted the LNO-type $PbNiO_3$ to be a multiferroic material with exceptionally large ferroelectric polarization of about 100 $\mu C/cm^2$.[13] It is therefore natural to expect that the *R*3*c* phase of $CdPbO_3$ may also possess interesting ferroelectric properties. Furthermore, though earlier resistivity measurements indicate insulating behavior for the perovskite-type phase of $CdPbO_3$,[14] the internal atomic positions and underlying electronic properties of both high-pressure $CdPbO_3$ polymorphs remain unknown.

In this work, we report the results of first-principle calculations on structural optimization, phase stability, and electronic and ferroelectric properties for the high-pressure perovskite- and LNO-type phases of $CdPbO_3$ by means of standard DFT and screened hybrid-functional methodologies. The paper is organized as follows: in the next section, we give a detailed description of the computational procedure. The results are presented and discussed in section III. Finally, the main outcomes of our study are summarized in section IV.

II. COMPUTATIONAL DETAILS

First-principles calculations presented in this work were carried out within standard and hybrid DFT using the Vienna ab initio simulation package (VASP).[15,16] In DFT the exchange-correlation energy functional was constructed according to the generalized gradient approximation (GGA) following the Perdew−Burke−Ernzerhof (PBE) parametrization scheme.[17] Due to the well-known difficulties of standard DFT in predicting the band gaps of semiconductors and insulators, we also employed the screened hybrid functional proposed by Heyd, Scuseria, and Ernzerhof (HSE),[18] which is constructed by suitably incorporating 25% of exact Hartree−Fock exchange in the short-range (SR) part of the DFT exchange (X) functional. The long-range (LR) part and the correlation (C) functional are treated by the PBE only, resulting in the following XC functional: $E_{XC}^{HSE} = 1/4E_X^{HF,SR,\mu} + 3/4E_X^{PBE,SR,\mu} + E_X^{PBE,LR,\mu} + E_C^{PBE}$ in which the parameter μ controls the decomposition of the Coulomb kernel into SR and LR contributions to the exchange. According to the HSE06 recipe, we set $\mu = 0.2$ Å^{-1}.[19] Hybrid functional, though computationally very demanding, has been proven to convey better structural data and improved electronic (band gap), magnetic, and ferroelectric properties with respect to standard DFT for transition-metal (TM) oxides.[13,20−23]

Full structural optimization was performed at both PBE and HSE levels, in which all lattice parameters and internal atomic positions were relaxed until the Hellmann−Feynman forces acting on each atom were less than 0.01 eV/Å and the energy difference between two consecutive iterations was less than 0.0001 eV. Brillouin zone integrations were performed with a Gaussian broadening[24] of 0.1 eV during all relaxations. For both geometry optimizations and static electronic structure calculations, the plane-wave energy cutoff was set to 600 and 400 eV within PBE and HSE, respectively. The *k*-point meshes over the total Brillouin zone were sampled by 8 × 6 × 8 and 8 × 8 × 8 Monkhorst−Pack grids[25] for the perovskite-type and LNO-type phases, respectively. Structure and charge density visualization and analysis were performed via the VESTA program.[26] Born effective charges were calculated using the linear-response technique within density functional perturbation theory,[27] whereas spontaneous polarization was evaluated using the Berry phase formalism.[28−30]

Pressure was simulated by changing the volume of the cell (the structure was optimized again under the constant volume constrain). To obtain the bulk modulus, the energy−volume (E−V) curves resulting from the structural optimization procedure at various volumes were fitted to the third-order Birch−Murnaghan equation of state (EOS)

$$E\left(V\right) = E_0 + 9V_0B_0/16\left\{\left[(V_0/V)^{2/3} - 1\right]^3 B_0' + \left[(V_0/V)^{2/3} - 1\right]^2\left[6 - 4(V_0/V)^{2/3}\right]\right\} \quad (1)$$

where B_0 is the bulk modulus at zero pressure, B_0' its first derivative, E_0 the minimum energy, and V_0 the volume at the minimum energy.[31] The pressure was obtained from the E−V graph by numerical differentiation of the Birch−Murnaghan EOS fit to the thermodynamic relationship $P = -\partial E/\partial V$. Since calculations were done at 0 K, the Gibbs free energy is equal to the enthalpy *H*, expressed as $H = E + PV$. Hence, we identified the phase transition pressure by comparing the enthalpy as a function of pressure. Due to the exceedingly high HSE computational cost, the EOS (eq 1) for the perovskite- and LNO-type structures was calculated at the PBE level only.

III. RESULTS AND DISCUSSION

A. Equilibrium Structures and Phase Stability. The perovskite-type phase of $CdPbO_3$ exhibits an orthorhombic $GdFeO_3$-type crystal structure with space group *Pnma* (No. 62). Its conventional unit cell, depicted in Figure 1, consists of four formula units (20 atoms). The most peculiar structural feature of this phase is the presence of a nonpolar distortion of the ideal cubic perovskite structure produced by the tilting of the oxygen octahedra around the cubic [110] axis. The PBE- and HSE-optimized equilibrium lattice constants, corresponding cell volume, internal atomic coordinates, bond lengths, and bond angles for the perovskite-type phase are listed in Table 1.

Table 1. Structural Parameters of Perovskite-Type $CdPbO_3$ in the *Pnma* Unit Cell Optimized by PBE and HSE[a]

Pv−$CdPbO_3$	PBE	HSE
a (Å)	5.839	5.739
b (Å)	8.379	8.210
c (Å)	5.750	5.639
V (Å^3/f.u.)	70.3	66.4
x_{Cd}	0.4539	0.4543
z_{Cd}	0.0069	0.0075
x_{O1}	0.5786	0.5732
z_{O1}	0.6264	0.6224
x_{O2}	0.1866	0.1886
y_{O2}	0.0698	0.0670
z_{O2}	0.3174	0.3157
Pb−O_1 (Å) × 2	2.2643	2.2058
Pb−O_2 (Å) × 2	2.1891	2.1394
Pb−O_2 (Å) × 2	2.2045	2.1549
Cd−O_1 (Å) × 1	2.3062	2.2764
Cd−O_1 (Å) × 1	2.3222	2.3070
Cd−O_2 (Å) × 2	2.2684	2.2494
Cd−O_2 (Å) × 2	2.8113	2.7574
Cd−O_2 (Å) × 2	3.0071	2.9355
Pb−O_1−Pb (deg)	135.39	137.04
Pb−O_2−Pb (deg)	137.68	139.06

[a] a, b, and c are the lattice constants, and V is the cell volume. Pb atoms are located in the Wyckoff position 4a (0, 0, 0), and Cd atoms are on 4c (x, 0.25, y). Two nonequivalent O atoms (O_1 and O_2) are positioned on 4c (x, 0.25, y) and 8d (x, y, z), respectively. Pb−O/Cd−O and Pb−O−Pb denote the corresponding bond lengths and bond angles, respectively. Experimental values: a = 5.887 Å, b = 8.061 Å, c = 5.676 Å, and V = 67.3 Å^3/f.u. are from ref 5.

Compared with the experiment,[5] the lattice constants obtained by the PBE calculations have an average deviation of 2.0%, with the highest overestimation being 3.9% for the **b** vector. As a consequence, the equilibrium volume is overestimated by roughly 4.5% at the PBE level. Obviously, HSE results are found to be in better agreement with the experiment, with an average error of less than 1.7%. In particular, the cell volume is well reproduced with an error of only 1.3%. The sizable difference between the Cd−O and the Pb−O bond lengths reflects a significant cooperative rotation of the PbO_6 octahedra, quantified further by the large reduction of the Pb−O_1−Pb (Pb−O_2−Pb) bond angle which is predicted to be 135.39° (137.68°) and 137.04° (139.06°) at the PBE and HSE levels, respectively.

The LNO-type phase of $CdPbO_3$ can be visualized as highly distorted perovskite with rhombohedral symmetry and an acentric space group *R*3*c* (No. 161). The primitive unit cell, shown in Figure 1, contains two formula units (10 atoms). This structure can be reached from the ideal cubic perovskite structure by two rather simple distortions: (i) counter-rotations of neighboring oxygen octahedra along the cubic [111] axis, and (ii) polar displacements of all the anion and cation sublattices relative to each other along the [111] direction. The optimized lattice constants, equilibrium volume, internal atomic positions, and corresponding bond lengths and bond angles calculated within both PBE and HSE functionals are collected in Table 2. To facilitate comparison with the measured data, calculated results are projected in the hexagonal setting. PBE delivers rather large lattice parameters (about 2.0% larger than experiment) and consequently a largely overestimated (6.3%) volume. As expected, inclusion of Fock exchange significantly improves the accuracy of the calculations: the error in the lattice parameters is reduced to ~0.11%, and the equilibrium volume, 68.3 Å^3 per formula unit (f.u.), is in excellent agreement with the experimental value (68.2 Å^3/f.u.). Similarly to the perovskite-like phase, HSE predicts a slightly smaller titling of the PbO_6 octahedra, which is mainly due to the different PBE and HSE equilibrium volumes. Overall, we can conclude that HSE conveys an improved description of the structural properties as compared to PBE and should therefore provide a good reference for future experiments aiming to determine the internal atomic positions of both $CdPbO_3$ polymorphs.

Table 2. Structural Parameters of $LiNbO_3$-Type $CdPbO_3$ Optimized via PBE and HSE[a]

LNO−$CdPbO_3$	PBE	HSE
a (Å)	5.787	5.679
c (Å)	14.992	14.681
V (Å^3/f.u.)	72.5	68.3
z_{Cd}	0.2795	0.2785
x_O	0.0511	0.0541
y_O	0.3616	0.3572
z_O	0.0650	0.0674
Pb−O (Å) × 3	2.1904	2.1364
Pb−O (Å) × 3	2.2857	2.2229
Cd−O (Å) × 3	2.2637	2.2333
Cd−O (Å) × 3	2.4649	2.5468
O−Pb−O (deg)	164.29	166.367
Pb−O−Pb (deg)	137.51	139.59

[a] To facilitate the comparison with experiment, the optimized results are presented in the hexagonal setting. The Wyckoff positions 6a and 18b are Cd (0, 0, z), Pb (0, 0, 0), and O (x, y, z). a and c are the hexagonal lattice constants, and V is the cell volume. Pb−O/Cd−O and Pb−O−Pb/O−Pb−O denote the corresponding bond lengths and bond angles, respectively. Experimental values: a = 5.681 Å, c = 14.640 Å, and V = 68.2 Å^3/f.u. are from ref 5.

The EOS for the perovskite- and LNO-type structures is shown in Figure 2, whereas the corresponding EOS parameters are listed in Table 3. The bulk modulus of the *Pnma* phase is larger than that of the *R*3*c* phase, indicating that the closely packed *Pnma* phase is more difficult to compress than the *R*3*c* one. From the E−V stability curves shown in Figure 2a, it can be seen that the *R*3*c* structure is energetically more favorable in a wide range of volumes and is thus predicted to be the most stable one under ambient conditions, whereas the orthorhombic *Pnma* phase is identified as a high-pressure phase as confirmed by the enthalpy−pressure curves shown in Figure 2b. This scenario is in accord with the experimental observations. Also, the calculated critical pressure at which the R3C → *Pnma* phase transition takes place, 9 GPa, is in good agreement with the measured value of 7−7.5 GPa.[5] We attribute this residual difference to the temperature effect, not included in our computational scheme (our calculations are performed at 0 K).

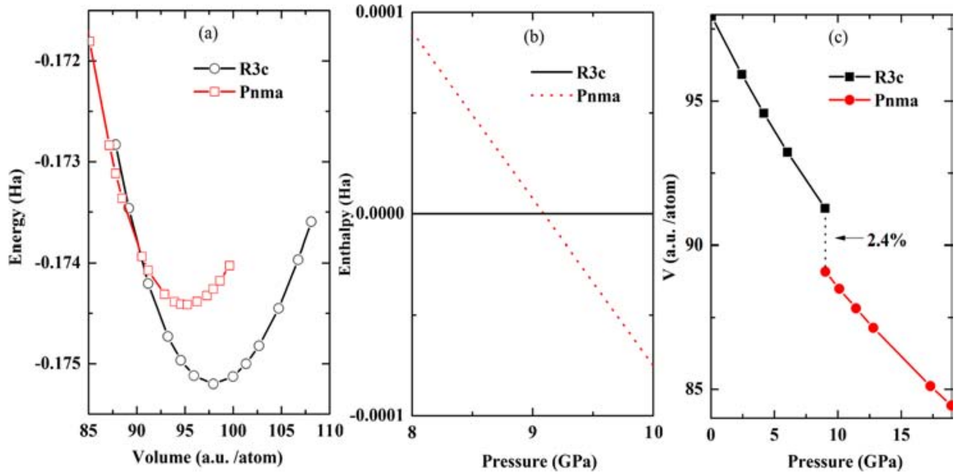

Figure 2. (a) PBE-calculated total energies as a function of volume for the perovskite- (*Pnma*) and LiNbO$_3$-type (*R3c*) phases. (b) Stability of phase vs pressure. (c) Relationship between pressure and volume for CdPbO$_3$. Pressure stability regions for the two different phases are also indicated.

Table 3. Equation of State Parameters for the Perovskite-(Pnma) and LiNbO$_3$-Type (R3c) CdPbO$_3$ Obtained at the PBE Level

structure	V_0 (Å/f.u.)	E_0 (eV/f.u.)	B (GPa)	B'
Pnma	70.38	−23.73	116.05	5.35
R3c	72.54	−23.84	108.38	4.35

According to the behaviors of the pressure−volume curves shown in Figure 2c, the R3C → *Pnma* phase transition is clearly first-order and involves a volume collapse of ∼2.4%.

B. Electronic Properties of the Perovskite-Type Phase. Standard DFT is known to be inadequate to describe the electronic properties of strongly correlated oxides. Indeed, the PBE functional predicts a metallic character for CdPbO$_3$ (see

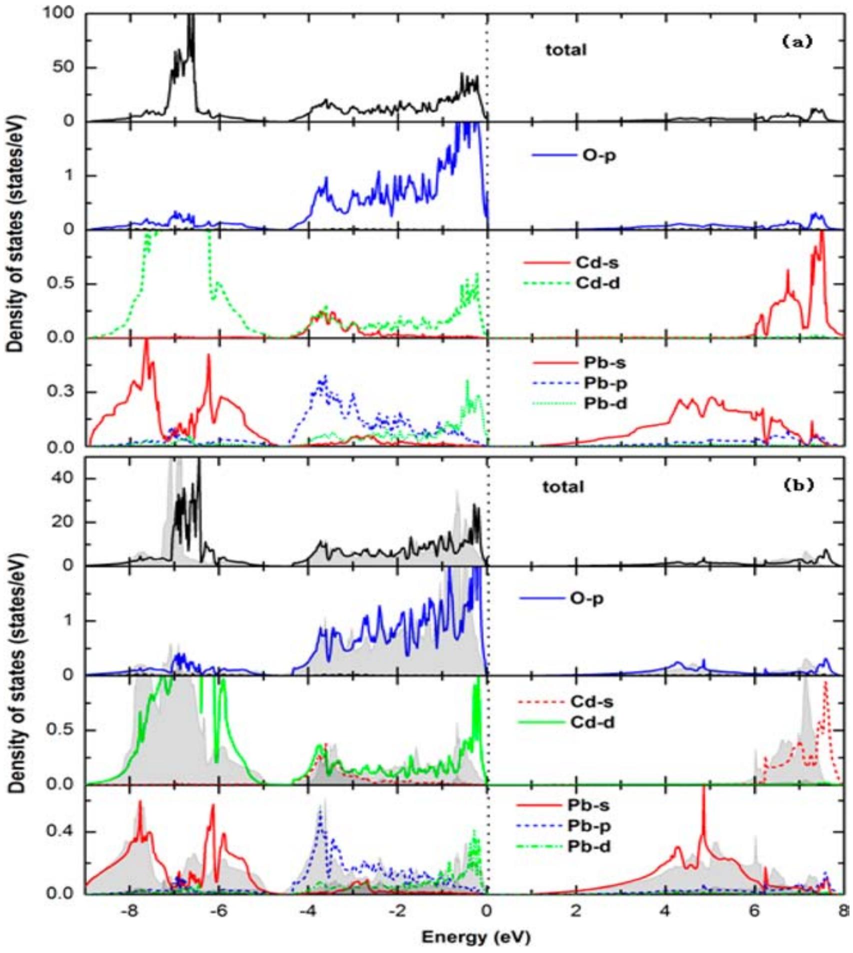

Figure 3. HSE-calculated total and partial density of states for CdPbO$_3$ in (a) the *Pnma* phase and (b) polar *R3c* (full lines) as well as reference centrosymmetric $R\overline{3}c$ (shadow) ones. Vertical dotted lines are set as the Fermi level.

Supporting Information), in clear disagreement with experiment.[14] Conversely, inclusion of the Fock exchange within the HSE functional correctly gives an insulating state with a band gap of ~1.17 eV as inferred from the electronic density of states (DOS) shown in Figure 3a. Therefore, in the following we will describe the electronic properties in terms of HSE only.

From the HSE-calculated results shown in Figure 3a, one can see that the bands between −9 and −5 eV are dominated by Cd 4d hybridized with part of O 2p and Pb 6s states whereas the highest occupied energy region is primarily formed by O 2p states with minor contributions from Cd 5s and Pb 6p states. Finally, the bottom of the conduction band is mainly made up by a mixture of Pb 6s and anion 2p states (the lowest energy region below −10 eV, not shown, is populated by O 2s and Pb 5d states). It is important to note that Pb does not donate all its valence electrons away, as a large portion of Pb s states is found below the Fermi level. Thus, similar to the case of $PbNiO_3$,[13] Pb is far from a nominal 4+ state.

C. Electronic and Ferroelectric Properties of the LNO-Type Phase. As mentioned above, the LNO-type $CdPbO_3$ has a rhombohedral structure with polar *R*3*c* space group. In this section, besides providing a detailed description of the electronic ground state of the LNO-type phase, we will report on the possible realization of ferroelectric behaviors connected with the observed polar crystal structure.

1. Electronic Properties. Similarly to the *Pnma* phase, also in this case PBE predicts a metallic character (see Supporting Information) whereas HSE finds a semiconducting ground state with a finite band gap of 0.94 eV. The HSE-calculated total and partial electronic DOS for LNO-type $CdPbO_3$ are shown in Figure 3b. Significant changes are observed by comparing the perovskite- (*Pnma*) and LNO-type (*R*3*c*) DOS: (i) the HSE value of the band gap decreases from 1.17 (*Pnma*) to 0.94 eV (*R*3*c*); (ii) there is a small but significant increase (0.4 eV) of the Pb 6s and O 2p bandwidths in the valence band of the rhombohedral structure with respect to the *Pnma* structure, which indicates an enhanced interaction between the Pb 6s and the O 2p orbitals in the *R*3*c* phase; (iii) this change in chemical bonding is accompanied by an expansion of the corresponding antibonding states in the bottom of the conduction band (this can explain the reduced band gap in the *R*3*c* phase); (iv) as a consequence of the structural transition, we also observe a sizable downward shift of the Pb 5d (0.3 eV) and Cd 4d (0.4 eV) bands.

The existence of an energy gap and significant covalent bonding between the cations and the oxygen in the acentric crystal structure are crucial prerequisites and necessary conditions for realization of ferroelectric behavior. In order to explore the possible realization of ferroelectricity in LNO-type $CdPbO_3$, in the following we will evaluate the spontaneous macroscopic polarization and discuss related ferroelectric properties.

2. Ferroelectric Properties. One of the basic features of ferroelectric materials is the spontaneous macroscopic polarization ***P***, which results upon application of an electric field and persists at zero field in two (or more) enantiomorphous metastable states of the crystal.[11] An accurate quantitative method for computing the polarization to all orders in displacement is the Berry phase theory (BPT) developed by Resta and King-Smith and Vanderbilt.[31−33] In this approach, the total polarization P_{tot} for a given material can be calculated as a summation of the ionic contribution P_{ion} and the electronic one P_{ele}. As there is an arbitrariness in the Berry phase represented by an integer multiple of the polarization quantum eR/Ω (where e is the charge of the electron, R is the primitive lattice vector along the polarization direction, and Ω is the unit cell volume), the spontaneous polarization should be calculated properly as a variation along an appropriate adiabatic path.

Here, the spontaneous polarization is calculated as the difference between the ferroelectric (FE) phase and a suitably centrosymmetric paraelectric (PE) one. Since the crystal structure of the high-temperature PE phase of $CdPbO_3$ has not been determined experimentally, we assume the rhombohedral $R\bar{3}c$ structure as the reference paraelectronic state in this case. The $R\bar{3}c$ structure, which is adopted by $LiNbO_3$ and $BiFeO_3$ in their PE phases,[8−12] can be derived from the ideal cubic perovskite structure by only a counter-rotation of the octahedra along the [111] axis. For the PE phase, we use the same volume and rhombohedral angle of the ferroelectric structure and further relax its internal atomic positions at the HSE level.

The HSE-calculated spontaneous polarization for LNO-type $CdPbO_3$ along the adiabatic insulating path is shown in Figure 4. The parameter λ represents the polar distortion of crystal structure between $R\bar{3}c$ ($\lambda = 0$) and $R3c$ ($\lambda = 1$) along the [111] direction. The polarization in the PE $R\bar{3}c$ phase is defined to be zero. From the results summarized in Figure 4 we derive the following information: (i) the ionic displacements (Figure 4a) induce a symmetry lowering along the PE to FE path and a concomitant decrease of the total energy. (ii) Both P_{ele} and P_{ion} (Figure 4b) grow monotonically with the polar distortion, giving rise to a total polarization P_{tot} of 52.3 μC/cm^2 (Figure 4c). This value is comparable to that of $ZnSnO_3$ (56.9 μC/cm^2)[32] but much smaller than that of $LiNbO_3$ (80.0 μC/cm^2),[9] $BiFeO_3$ (83.53 μC/cm^2),[11] and PbNiO3 (95.5 μC/cm^2).[13] (iii) In Figure 4c we also compare the polarization obtained through the BPT with the corresponding point charge model (PCM) value.[33] The negligible difference between the calculated P_{tot} and P_{PCM} is often indicative of a predominantly ionic character.

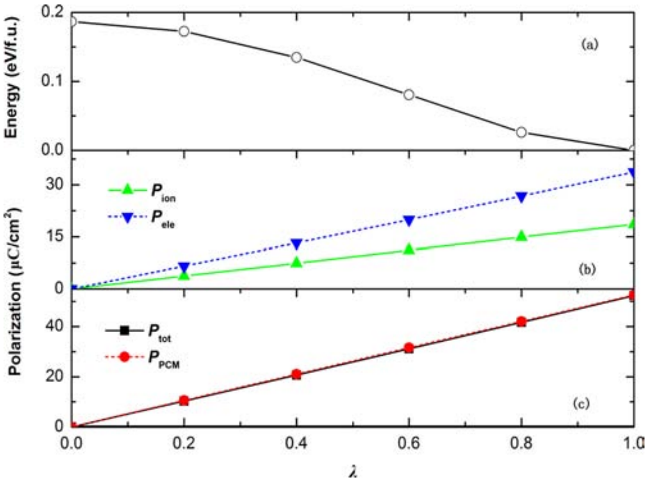

Figure 4. HSE-calculated total energy E, ionic P_{ion}, electronic P_{ele}, and total polarization P_{tot} are illustrated as a function of the polar distortion λ along a ferroelectric switching path going from the reference paraelectric $R\bar{3}c$ structure ($\lambda = 0$) to the ferroelectric $R3c$ one ($\lambda = 1$). The spontaneous polarization estimated from the point charge model (P_{PCM}) is also given for comparison.

An alternative way to evaluate (within a lower degree of accuracy) the polarization is through the Born effective charge

(BEC) and the polar displacements by using the expression $P_\alpha = 1/\Omega \sum_{\kappa,\beta} Z^*_{\kappa,\alpha\beta} \Delta u_{\kappa,\beta}$, where $\Delta u_{\kappa,\beta}$ is the displacement of atom k along direction β from the PE to the FE phase and $Z^*_{\kappa,\alpha\beta}$ is the Born effective charge tensor of atom k.[9] The BEC tensors of each ion in the FE ($R3c$) and reference PE ($R\overline{3}c$) structure of $CdPbO_3$ are calculated using the linear-response formalism within the PBE approach. The results are summarized in Table 4. On the basis of the BEC tensor of the FE phase (Table 4), the polarization is estimated to be 56.8 and 53.8 $\mu C/cm^2$ using, respectively, the PBE- and HSE-optimized geometries. These results are in close agreement with the Berry phase estimate (52.3 $\mu C/cm^2$) and corroborate further our calculations.

Table 4. Born Effective Charge (in atomic units) Cd, Pb, and O_1, O_2, and O_3 of $CdPbO_3$ in the Reference Paraelectric $R\overline{3}c$ and Ferroelectric $R3c$ Phases, Calculated via PBE

	paraelectric phase			ferroelectric phase		
Cd	2.67	0.00	0.00	2.56	−0.20	0.00
	0.00	2.67	0.00	0.21	2.57	0.00
	0.00	0.00	2.10	0.00	0.00	2.28
Pb	4.42	0.64	0.00	4.44	0.76	0.00
	−0.64	4.42	0.00	−0.73	4.43	0.00
	0.00	0.00	4.59	0.00	0.00	4.64
O_1	−2.24	−0.19	−0.43	−2.26	−0.22	−0.17
	−0.19	−2.47	−0.75	−0.26	−2.39	−0.63
	−0.43	−0.75	−2.22	−0.09	−0.76	−2.29
O_2	−2.58	0.00	0.87	−2.56	0.09	0.63
	0.00	−2.14	0.00	0.04	−2.09	0.16
	0.87	0.00	−2.22	0.70	0.30	−2.29
O_3	−2.25	0.19	−0.44	−2.15	0.19	−0.46
	0.19	−2.47	0.75	0.16	−2.50	0.46
	−0.44	0.75	−2.22	−0.61	0.45	−2.29

After predicting the onset of a large spontaneous polarization in LNO-type $CdPbO_3$, we now turn to discussion of the mechanism behind this FE behavior. As already pointed out, the polar distortions in LNO−$CdPbO_3$ are very similar to those observed in LNO−$PbNiO_3$.[13] In LNO−$PbNiO_3$ the FE transition is driven by the strong Pb−O covalent interactions, similarly to what was reported for $BiFeO_3$ and $PbTiO_3$. By analogy, we expect that also in this case the ferroelectric mechanism can be assimilated to the partial covalency of some bonds.

First, we describe in more detail the ferroelectric structural distortions by comparing the energy path associated with the PE to FE transition. As mentioned above, development of the spontaneous polarization originates from the relative displacement of all cations and anions along the [111] direction (i.e., the c-axis direction in the hexagonal setting). With respect to the centrosymmetric PE configuration and keeping the Pb atoms fixed at the origin, the Cd atoms in the FE phase are shifted along the 3-fold axis by 0.442 Å while O atoms move approximately in the opposite direction by 0.275 Å. As already pointed out, the O atoms not only move along the c axis but have sizable displacements along axes a and b. The calculated potential energy path of LNO−$CdPbO_3$ as a function of the atomic displacements from the centrosymmetric structure to the polar one is displayed in Figure 5, decomposed over Cd-only, O-only, and combined Cd + O displacements. The abscissa indicates the amount of displacements as a fraction of the PE to FE amplitude. When considering the combined Cd + O contributions, the potential energy curve has the double-well shape typical of ferroelectric materials, indicating the special role played by these atoms in determining the ferroelectric transition. The total energy gain associated with the Cd + O polar distortion is 229 meV/f.u., comparable to the corresponding ferroelectric energy gain in $LiNbO_3$ (249 meV/f.u.)[8] and $PbTiO_3$ (200 meV/f.u.)[34] (twice smaller than the value predicted for $BiFeO_3$[11]). It is important to underline that the distinct Cd and O displacements do not lead to any sizable energy again. It is the combined motion of Cd + O atoms along the [111] direction that determines the PE to FE transition.

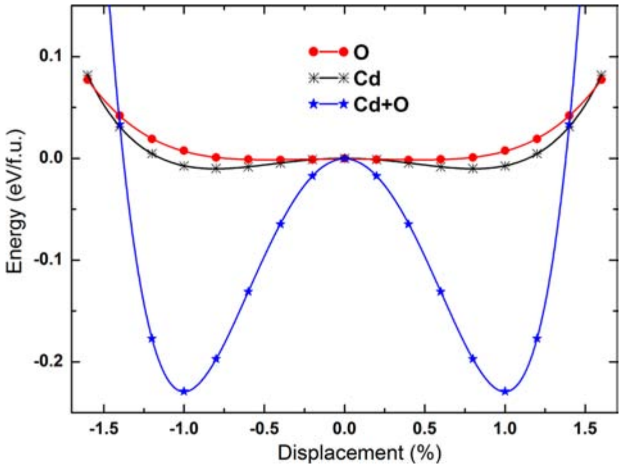

Figure 5. PBE-calculated potential-energy surfaces vs atomic displacements from their centrosymmetric positions. Abscissa indicates the amount of displacements as a fraction of the paraelectric to ferroelectric amplitude. Energy minimum corresponds to the ferroelectric $R3c$ structure.

To gain further insight on the ferroelectric mechanism in LNO-type $CdPbO_3$, we now describe the nature of the chemical bonding on the basis of (i) charge density analysis, both electronic density and charge-transfer distribution, (ii) BEC, (iii) DOS, and (iv) electron localization function (ELF).

Figure 6 shows the calculated electron densities and charge-transfer distribution in a plane containing Cd, Pb, and O atoms. From the electronic density plot in Figure 6 (left), it is obvious that in the ferroelectric $R3c$ phase the bonding interaction between Pb and O as well as between Cd and O is not purely

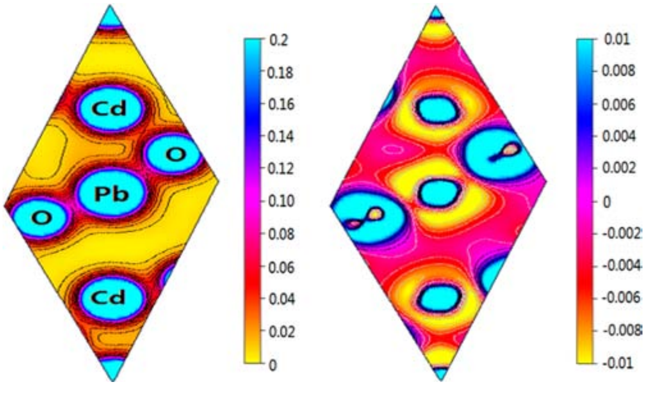

Figure 6. PBE-calculated valence-electron charge density (left) and charge-transfer (right) plots for $LiNbO_3$-type $CdPbO_3$. In the charge-transfer plot, the solid line (black) is applied to lines of positive values and dashed line (gray) to lines of negative values.

ionic. This is also in line with the conclusions that can be outlined for analysis of the BEC listed in Table 4: comparing the PE and FE data, we observe a global increase of the Cd, Pb, and O charges in the FE state, especially along the ferroelectric polarization [111] direction. This reveals that the distortions in the ferroelectric phase induce appreciable change in covalency. The directional nature of the charge density distribution is generally an indicator for the existence of finite covalent bonding. In Figure 6 (right), the charge-transfer plot clearly shows that electrons transfer from both Pb and Cd atoms to the oxygen sites, highlighting an ionic-like character. On the other hand, the anisotropic distribution of charge transfer in $CdPbO_3$ confirms the presence of covalent bonding between the Cd atoms and the oxygens and between the Pb atoms and its oxygen neighbors. We can thus conclude that the chemical bonding in the ferroelectric *R*3*c* phase has a mixed covalent–ionic character, similarly to what has been observed in most perovskite oxides, such as $LiNbO_3$[9] and $BiFeO_3$.[11]

The important role of covalency effects in the FE transition is also reflected in the DOS. In Figure 3b we compare the FE DOS with those of the reference PE phase. Although the electronic structures of the *R*3*c* and $R\bar{3}c$ phases are similar, there are some significant and relevant differences. In particular, going from the PE to the FE phase there is an upward shift of the center of mass of the Cd 4d manifold resulting in an enhanced Cd–O admixture right below E_F, and a broadening of the Pb 6s orbitals which also contributes to strengthening the Pb–O covalent interaction. This effect is often referred as stereochemical activity of the A-site cation and is invoked to interpret the ferroelectric behavior lone-pair-like ferroelectrics such as $BiFeO_3$,[10−12] $BiMnO_3$,[35,36] and $PbTiO_3$.[37]

Finally, we examine the ELF, which is a useful tool to distinguish the nature of different types of bonding in solid state systems.[38] The HSE calculated valence ELF contours are shown in Figure 7 for a plane containing Cd, Pb, and O atoms within the FE and reference PF structures. The negligibly small value of the ELF in the interstitial region between the various atoms indicates the existence of dominant ionic-like bonding in both phases. In comparison with the PE phase, the absence of an inversion center in the ferroelectric phase and the associated atomic displacements induce a strong asymmetric ELF along the [111] direction and a substantial increase of covalent-like nature of the Pb–O and Cd–O bonding. Along with the DOS analysis discussed above, this, in turn, clarifies further the nature of the covalent bonding between the Pb 6s and the O2p orbitals and between the Cd 4d and the O 2p orbitals in the ferroelectric *R*3*c* structure.

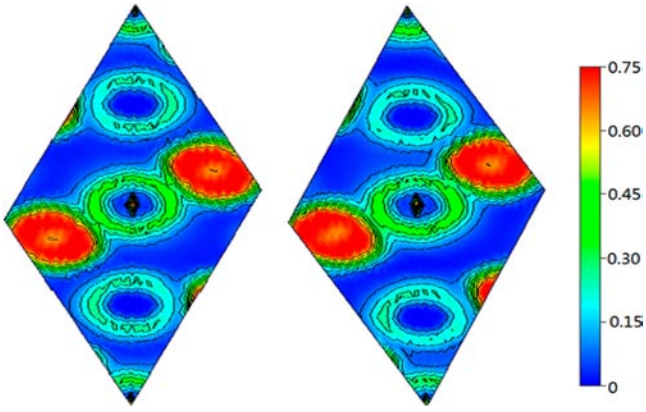

Figure 7. HSE-calculated valence electron localization function (ELF) contour of $CdPbO_3$ in the reference paraelectric $R\bar{3}c$ (left) and ferroelectric *R*3*c* (right) structures. Both contours are plotted up to 0.75 a_0^{-3} (a_0, Bohr radius) with an interval of 0.08. Atom labels in the planes are same as that in Figure 6.

In conclusion, all our findings point out that the most relevant electronic change associated with the PE–FE transition is the substantial enhancement of the Pb–O and Cd–O covalent interactions, which is the driving mechanism behind the ferroelectric instability. LNO–$CdPbO_3$ can be thus considered a proper ferroelectric similar to $PbNiO_3$ and $BiFeO_3$. The anisotropic nature of electronic charge at the Pb sites (see Figures 6 and 7) allows the off-centering displacement of the Pb atom in the oxygen octahedra. This induces a cooperative motion of the Cd atoms along the [111] direction due to large direct and oxygen-mediated A–B repulsions. Cd displacements transform CdO_3 complexes in the reference PE phase into CdO_6 cages in the FE phase, which explains the obvious change of the spectral weight of the Cd 4d states during the ferroelectric transition (see Figure 3b). The cooperative displacements of all cations and anions ultimately lead to formation of FE polarization in the LNO-type phase. This is clearly reflected in the structural distortion which predominantly involves the coupled motion of the Cd and O atoms along the polar direction.

IV. SUMMARY

We performed a first-principles study of the structural and electronic properties for the perovskite-type (space group *Pnma*) and LNO-type (space group *R*3*c*) high-pressure polymorphs of $CdPbO_3$ using first-principles calculations within the standard DFT and hybrid-functional HSE approximation. We predicted the ferroelectric nature of the LNO-type phase and discussed the origin of the ferroelectric behavior in terms of the BEC, DOS, charge density isosurfaces, and electronic localization function analysis. The most relevant results of our computational study can be summarized as follows.

(1) Structural optimization: our PBE/HSE-optimized lattice parameters for both high-pressure $CdPbO_3$ polymorphs are in good agreement with the experimental lattice parameters. We also fully optimized the internal atomic positions. Besides serving as a reference for future experimental studies, this structural analysis turned out to be essential to understand the ferroelectric behavior.

(2) Pressure-induced structural transition: our computed critical pressure for the *R*3*c*–*Pnma* phase transition, 9 GPa, is in very good agreement with the measured value, 7–7.5 GPa. The phase transition is confirmed to be first order with a volume collapse of ~2.4%. The *R*3*c* structure is predicted to be stable under ambient conditions, and the *Pnma* structure can be viewed as a high-pressure phase of $CdPbO_3$. This scenario is very consistent with the experimental findings.

(3) Electronic character: HSE is capable to reproduce an insulating ground state for both phases, whereas PBE delivers a poorly metallic solution, in disagreement with experiment.

(4) Ferroelectricity: the LNO-type phase was predicted to be a potential ferroelectric material. On the basis of the Berry phase formalism, the spontaneous polarization was estimated as 52.3 $\mu C/cm^2$ along the [111] direction,

which is in magnitude comparable to that of $ZnSnO_3$. The calculated potential-energy surfaces indicate that the ferroelectric phase transition is not driven by the displacements of the cadmium or oxygen alone but rather from the combined Cd + O displacements along the polar direction. The overall energy gain associated with the PE → FE transition is estimated to be 229 meV/f.u.

(5) The driving force inducing the onset of a spontaneous polarization in the ferroelectric phase of $CdPbO_3$ is the enhanced Cd−O and Pb−O covalent interactions across the ferroelectric transition, a mechanism similar to that reported for $BiFeO_3$ and $PbNiO_3$, though in this case the role of lone-pair-like stereoactive electrons seems less crucial.

■ ASSOCIATED CONTENT

Ⓢ Supporting Information

This material is available free of charge via the Internet at http://pubs.acs.org.

■ AUTHOR INFORMATION

Corresponding Author

*E-mail: fmgao@ysu.edu.cn.

Notes

The authors declare no competing financial interest.

■ ACKNOWLEDGMENTS

This work was supported by the National Natural Science Foundation of China (Grant Nos. 21071122 and 21201148) and Natural Science Foundation of Hebei (Grant No. B2011203121). X.H. and C.F. are grateful to support from FP7 EU-INDIA grant ATHENA. Part of the computations was performed on the Vienna Scientific Cluster.

■ REFERENCES

(1) Goldschmidt, V. M. *Naturwissenschaften* **1926**, *14*, 477−485.

(2) Shannon, R. D. *Acta Crystallogr., Sect. A* **1976**, *32*, 751−767.

(3) Goodenough, J. B.; Kafalas, J. A.; Longo, J. M. *High pressure synthesis. Preparative Methods in Solid State Chemistry*; Academic Press: New York, 1972.

(4) Inaguma, Y.; Tanka, K.; Tsuchiya, T.; Mori, D.; Katsumata, T.; Ohba, T.; Hiraki, K.; Takahashi, T.; Saitoh, H. *J. Am. Chem. Soc.* **2011**, *133*, 16920−16929.

(5) Inaguma, Y.; Yoshida, M.; Tsuchiya, T.; Aimi, A.; Tanaka, K.; Katsumata, T.; Mori, D. *J. Phys.: Conf. Ser.* **2010**, *215*, 012131.

(6) Halasyamani, P. S.; Poeppelmeier, K. R. *Chem. Mater.* **1998**, *10*, 2753−2769.

(7) Ok, K. M.; Chi, E. O.; Halasyamani, P. S. *Chem. Soc. Rev.* **2006**, *35*, 710−717.

(8) Inbar, I.; Cohen, R. E. *Phys. Rev. B* **1996**, *53*, 1193−1204.

(9) Veithen, M.; Ghosez, P. *Phys. Rev. B* **2002**, *65*, 214302.

(10) Neaton, J. B.; Ederer, C.; Waghmare, U. V.; Spaldin, N. A.; Rabe, K. M. *Phys. Rev. B* **2005**, *71*, 014113.

(11) Ravindran, P.; Vidya, R.; Kjekshus, A.; Fjellvåg, H.; Eriksson, O. *Phys. Rev. B* **2006**, *74*, 224412.

(12) Stroppa, A.; Picozzi, S. *Phys. Chem. Chem. Phys.* **2010**, *12*, 5405−5416.

(13) Hao, X. F.; Stroppa, A.; Picozzi, S.; Filippetti, A.; Franchini, C. *Phys. Rev. B* **2012**, *86*, 014116.

(14) Yamamoto, A.; Khasanova, N. R.; Izumi, F.; Wu, X.-J.; Kamiyama, T.; Torii, S.; Tajima, S. *Chem. Mater.* **1999**, *11*, 747−753.

(15) Kresse, G.; Hafner, J. *Phys. Rev. B* **1993**, *47*, 558−561.

(16) Kresse, G.; Furthmuller, J. *Comput. Mater. Sci.* **1996**, *6*, 15−50.

(17) Perdew, J. P.; Burke, K.; Ernzerhof, M. *Phys. Rev. Lett.* **1996**, *77*, 3865−3868.

(18) Heyd, J.; Scuseria, G. E.; Ernzerhof, M. *J. Chem. Phys.* **2003**, *118*, 8207−8215.

(19) Krukan, A. V.; Vydrov, O. A.; Izmaylov, A. F.; Scuseria, G. E. *J. Chem. Phys.* **2006**, *125*, 224106.

(20) He, J.; Chen, M.-X.; Chen, X.-Q.; Franchini, C. *Phys. Rev. B* **2012**, *85*, 195135.

(21) Hong, J.; Stroppa, A.; Íñiguez, J.; Picozzi, S.; Vanderbilt, D. *Phys. Rev. B* **2012**, *85*, 054417.

(22) Franchini, C.; Archer, T.; He, J.; Chen, X.-Q.; Filippetti, A.; Sanvito, S. *Phys. Rev. B* **2011**, *83*, 220402.

(23) Franchini, C.; Sanna, A.; Marsman, M.; Kresse, G. *Phys. Rev. B* **2010**, *81*, 085213.

(24) Elsässer, C.; Fähnle, M.; Chan, C. T.; Ho, K. M. *Phys. Rev. B* **1994**, *49*, 13975−13978.

(25) Monkhorst, H. J.; Pack, J. D. *Phys. Rev. B* **1976**, *13*, 5188−5192.

(26) Momma, K.; Izumi, F. *J. Appl. Crystallogr.* **2008**, *41*, 653−658.

(27) Gonze, X.; Lee, C. *Phys. Rev. B* **1997**, *55*, 10355−10368.

(28) Resta, R. *Rev. Mod. Phys.* **1994**, *66*, 899−915.

(29) Vanderbilt, D.; King-Smith, R. D. *Phys. Rev. B* **1993**, *48*, 4442−4455.

(30) King-Smith, R. D.; Vanderbilt, D. *Phys. Rev. B* **1993**, *47*, 1651−1654.

(31) Birch, F. *Phys. Rev.* **1947**, *71*, 809−824.

(32) Nakayama, M.; Nogami, M.; Yoshida, M.; Katsumata, T.; Inaguma, Y. *Adv. Mater.* **2010**, *22*, 2579−2582.

(33) Stroppa, A.; Marsman, M.; Kresse, G.; Picozzi, S. *New J. Phys.* **2010**, *12*, 093026.

(34) Picozzi, S.; Yamauchi, K.; Sanyal, B.; Sergienko, I. A.; Dagotto, E. *Phys. Rev. Lett.* **2007**, *99*, 227201.

(35) Seshadri, R.; Hill, N. A. *Chem. Mater.* **2001**, *13*, 2892−2899.

(36) Hill, N. A.; Rabe, K. M. *Phys. Rev. B* **1999**, *59*, 8759−8769.

(37) Cohen, R. E. *Nature* **1992**, *358*, 136−138.

(38) Savin, A.; Nesper, R.; Wenget, S.; Fassler, T. F. *Angew. Chem., Int. Ed.* **1997**, *36*, 1808−1832.